
Multi-Stiffness Matching Method of Raft Isolator for Avoiding Resonance of Superconducting Motor Based on Rbf Agent Model and Particle Swarm Optimization Algorithm

Zekun Jia

School of Naval Architecture, Ocean and Energy Power Engineering, Wuhan University of Technology, Wuhan 430063, China.

Yang Xiang

Key Laboratory of High Performance Ship Technology (Wuhan University of Technology), Ministry of Education, Wuhan 430063, China. E-mail: yxiang@whut.edu.cn

Yong Zhou

Wuhan Institute of Marine Electric Propulsion, Wuhan 430063, China.

(Received 24 July 2024; accepted 23 November 2024)

The multi-stiffness matching method of raft isolator based on RBF (Radial Basis Function) agent model and particle swarm optimization algorithm is proposed to solve the resonance of superconducting motor using as main propulsion plant. Firstly, the modeling methods for the end-winding of high-temperature superconducting motor stator coils are investigated, including the equivalent density method, additional mass method, and non-simplification method. Additionally, the optimal modeling scheme is selected by comparing with experimental results. An accurate vibration prediction model for the superconducting motor's raft system is established. Subsequently, based on finite element power flow analysis, the transfer paths of electromagnetic forces in the motor structure and the distribution characteristics of vibration energy on the raft are studied. Based on this analysis, a vibration isolator grouping scheme is designed in accordance with the law of vibration transmission of electromagnetic excitation force. Furthermore, a vibration response agent model of the superconducting motor-raft-shell system is constructed using the RBF network. An optimal stiffness matching scheme is formulated through a multi-objective particle swarm optimization algorithm. The results indicate that the motor excitation force predominantly propagates through the armature frame to the intermediate raft frame and subsequently to the shell. By employing the optimization algorithm, the stiffness distribution of the vibration isolator group is configured to be softer in the middle and stiffer at both ends. Finally, the vibration isolation effect is enhanced by 8.6 dB while maintaining the vibration level of the motor base plate constant.

1. INTRODUCTION

Superconducting motors exhibit superior power density and efficiency compared to conventional DC motors,¹ rendering them highly promising for a wide range of applications. The internal structure of superconducting motors, including the stator and coil configuration, is intricate. Due to factors such as the presence of coolant and the stacked coupling of silicon steel sheets, the modal frequencies of the stator assembly are low and concentrated.² Particularly, during high-power, low rotational speed operations as a propulsion motor, these motors experience high-amplitude electromagnetic excitation forces and clearly discernible low-frequency line spectra, leading to resonance phenomena in the low-frequency range that hinder effective dissipation of vibration energy. Consequently, a detailed analysis of the electromagnetic force transmission path in high-temperature superconducting motors is imperative to understand the excitation force transmission law and devise a rational and efficient control strategy.

The precise modeling of superconducting motors is essen-

tial for the analysis of vibration characteristics. Given the intricate structure of the stator and coil winding in superconducting motors, it is imperative to appropriately simplify the model and validate it through modal testing to ensure its accuracy. Wang³ conducted an analysis of the internal structure of the stator to investigate the effects of various factors on its modal characteristics. A high-precision stator model was developed and subsequently validated for accuracy through experimental results. Chai⁴ used the Voigt-Reuss formula combined with the equivalent method of empirical coefficients to establish the finite element model of the windings and the seat in the stator system and compared it with the test to verify the accuracy of the model. In the finite element calculation, to establish a high-precision stator simulation model. Yin⁵ combined the modal test to correct the equivalent parameters of the stator core and winding materials to obtain a high-precision simulation model and proposed a method for the correction of the equivalent material parameters.

For each structure of conventional motor stator systems, the

simplification method has been refined, enabling the development of numerical simulation models that closely align with actual test results. However, superconducting motors involve complex structures, including coolant channels and stacked silicon steel sheets. Therefore, further exploration is needed to simplify and model the superconducting motor stator assembly.

The structure of superconducting motors is complex and the mass distribution is uneven, making the study of vibration transmission paths a major focus. Hu⁶ established a transmission path analysis model for propeller motors and combined it with vibration test results to determine that the main transmission path for propeller motors is located at the motor support plate. The prediction of vibration energy distribution and transmission paths often adopts TPA and structural intensity analysis methods. Li⁷ conducted a contribution analysis on a marine reducer and identified the main transmission path of a double-layered enclosure based on force transmission rate analysis, which is the isolator. Additionally, Yang⁸ used a combination of classical TPA and power flow methods to analyze the main transmission path from the main engine to the shell and seawater pump. They pointed out that the isolator is the main transmission path for low-frequency spectrum and it affects the dissipation of vibration energy. Wang⁹ proposed a Modal Expansion combined with finite element method for structural intensity analysis to analyze the vibration energy transmission path of a cantilever plate under thermal load. Zhu¹⁰ analyzed the transmission path of a fiber composite material plate using the structural intensity method and visualized the results, demonstrating the distribution and transmission patterns of vibration energy. It can be seen that the structural intensity method is widely used in the analysis of vibration energy distribution and transmission paths, and its technical means are becoming mature. However, there is relatively limited research on the analysis of the transmission path of electromagnetic excitations from superconducting motors to the shell structure.

The vibration source of superconducting motors is mainly the electromagnetic force acting on the stator. Under low-speed conditions, the frequency of the excitation force is often within the low frequency range of 100 Hz, and due to the elasticity of the installation of superconducting motors, the modal frequency corresponding to the overall vibration is also below 100 Hz. The excitation frequency of electromagnetic force is close to the frequency of motor installation, which is prone to resonance phenomenon. Secondly, low-frequency vibrations have longer wavelengths and can more easily propagate to various components of the motor, thereby increasing the difficulty of control. Although, the design of the plate spring structure for vibration isolation¹¹ makes the motor in a wide range of frequencies within the vibration reduction obvious, the low-frequency does not have the effect, due to the presence of resonance in the low-frequency, so the effect of plate spring damping failure.¹² For the problem of motor low-frequency vibration control, scholars mostly adopt active control methods to control the motor excitation source: Li¹³ based on the inverse system decoupling method and μ -synthesis of the control of the motor bearing rigid rotor vibration in the low and high frequency for effective control; Zhao¹⁴ based on the fractional-order proportional-integral differential controller to achieve real-time control of the motor vibration of the low-frequency; Li¹⁵ proposed an optimization measure combin-

ing active disturbance control (ADRC) and random frequency space vector pulse width modulation to suppress the sideband vibration of the motor, which was verified by simulation. For the conventional motor active control to achieve a more significant control effect, but due to the cost of the active control scheme and failure rate and other issues, the application of a large superconducting motor platform is less.

In the field of ships, large mechanical equipment mostly adopt a double-layer vibration isolation system for control in the transmission path. Wang¹⁶ designed a double-layer vibration isolation system based on electromagnetic control, which has a better dissipation effect on low-frequency vibration. Wen¹⁷ designed a truss-type CFRP raft that effectively reduces the vibration transmitted to the base. He¹⁸ combined with the Functional Gradient Material (FGM) to design a double-deck raft structure, investigated the influence of material, structural parameters, stiffness and damping on the vibration response of FGM double-deck raft, laying a foundation for the subsequent optimization design. Li¹⁹ established a 12-degree-of-freedom quasi-zero-stiffness floating raft system high-dimensional mathematical model, which has an excellent vibration isolation performance relative to traditional linear vibration isolation in the middle and high frequency bands. Wang²⁰ based on the genetic optimization algorithm to optimize the design of a periodic structure raft, by reducing the power flow through the periodic structure making the periodic structure has a wider resistive band region. For vibration control of large equipment, a double-layer isolation system can effectively control the energy transmitted from the equipment excitation source to the shell. However, the stiffness of the isolator was selected as a set of identical stiffness without considering the influence of equipment mass and its vibration energy distribution characteristics, which limits the isolation effect.

While the majority of scholars tend to concentrate on the simplified modeling and vibration analysis of conventional electrical equipment, the unique stator structure of superconducting motors presents distinct challenges. Notably, the low-frequency electromagnetic excitation force exhibits complex transmission paths within superconducting motors. Moreover, the conventional approach of selecting vibration isolator stiffness in a singular manner fails to sufficiently address the low-frequency vibration isolation efficiency in double-layer isolation systems. Hence, this study focuses on developing an optimal stiffness matching solution for the vibration isolation system in the superconducting motor-raft-shell configuration to reduce the transfer of vibration energy to the shell. Section 2 delves into the analysis of stator assembly modes, with validation of the simulation model accuracy through experimental testing. Section 3 involves the development of a finite element model for the superconducting motor-raft-shell system, followed by an analysis of vibration characteristics. Investigation into the transmission pathway of electromagnetic force within the superconducting motor-raft-shell system model is conducted in Section 4. Section 5 implements a multi-objective, multi-parameter optimization design based on the RBF neural network for the motor-raft-shell system model, establishing an agent model to formulate an optimal stiffness matching scheme. Finally, Section 6 presents the study's conclusion.

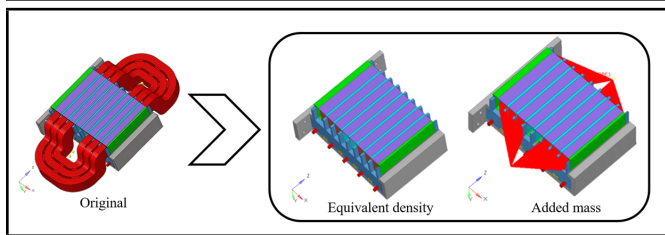


Figure 1. FE model of different modeling method.



Figure 2. Test Site Layout.

Table 1. Frequency of winding ends under three different states.

Order	Frequency /Hz		
	Original	Added mass	Equivalent density
1	757.56	768.66	—
2	1076.58	1068.64	677.518
3	1119.82	1107.39	810.01
4	1671.13	1670.76	1792.76
5	1700.34	1703.59	1712.43
6	1823.08	1841.91	1283.76

2. MODEL AND VALIDATION

To verify simplified modeling methods for the stator subsystem, we compared the additional mass and equivalent density methods, identified the most suitable one, and established a finite element model for the superconducting motor-shell system.

2.1. Analysis of Stator Coil Modeling Method

The scaled stator was created by cutting the whole stator circumferentially, then scaling axially by 1 : 2 and circumferentially by 2 : 3, with coil thickness and stator slot size unchanged. Simplifying the end model by ignoring the volume and shape of the winding end is necessary. Two methods were proposed: the equivalent density method, which adjusts coil density, and the added mass method, which attaches end winding mass to the linear coil. The FE models under different modeling methods are shown in Fig. 1. The three models were imported into ANSYS for modal simulation calculation, and the modal vibration mode order was calculated. The modal vibration mode of the additional mass method was taken as the reference. The frequency of each order of winding end under three different states is shown in Table 1: It can be seen from the table that the natural frequency error between the stator model established by using the additional mass method and the original model was small, while the natural frequency difference between the stator model established by using the equivalent density method and the original model was only small in the 4th and 5th order, and large in the 2nd and 3rd order. In addition, the stator model established by the equivalent density method will have the phenomenon of order disorder and individual order disappearance. The main reason was that the density of the winding established by the equivalent density method is uniform, which destroys the mass distribution law of the original structure.

2.2. Scaled Stator Modal Test

To further simplify the accuracy of some parts in the modeling process and the effectiveness of the modeling method, the hammering method was used for the modal test of the scaled stator. The hammering method was used for the modal test of

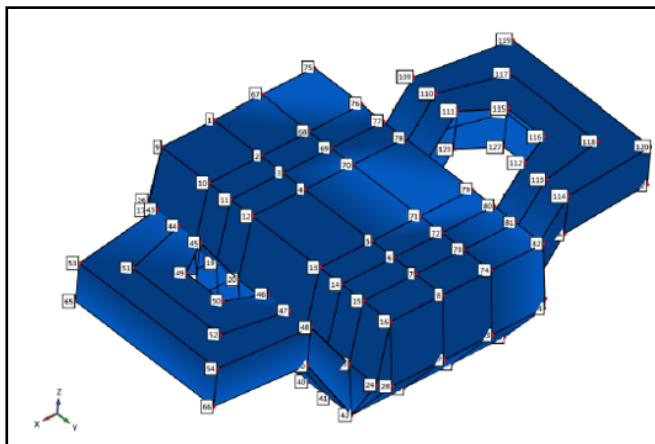


Figure 3. Measurement Point Layout Diagram.

the scaled stator. DHDAS test system was adopted for data acquisition, Lance acceleration sensor was adopted as the sensor, and the model of force hammer was LC-60 kN. During the test, the suspension method was adopted to make the scaled stator in a free state. The test site diagram is shown in this Fig. 2: During the experiments, it was observed that when there was an incomplete rigid connection between the coil and the stator core, as well as between the core and the fastening stiffness, the vibration characteristics of the system changed. Specifically, this incomplete rigidity led to increased error in certain orders due to insufficient mechanical stiffness, which caused shifts in the resonance frequency or increased vibration amplitude.

The upper and lower panels were each equipped with 32 measurement points. Given that the scaled-down stator lacked coils in its central section, resulting in a hollow structure, most measurement points are arranged directly above and below the coil positions. For the coil ends, six measurement points were arranged above and below each turn of the coil at each side. The remaining measurement points were primarily positioned at the corners to approximate the overall structure of the scaled-down stator. The arrangement of measurement points and the test model for the scaled-down stator are shown in Fig. 3. The modal test results of the scaled-down stator were compared with those of the finite element model. The first four modal shapes were extracted, and the comparison results are shown in Fig. 4. The modal test results are compared with the finite element simulation results, and the results are shown in Table 2. It can be seen from the table that although there are some errors between the simulation and test, the error between the simulation and the test of individual orders is slightly more than 10 %. The error comes from the incomplete rigid connection between the coil and the stator core and between the core and the fastening stiffness, and the error range of other orders is within 10 %. At the same time, it shows the effectiveness of

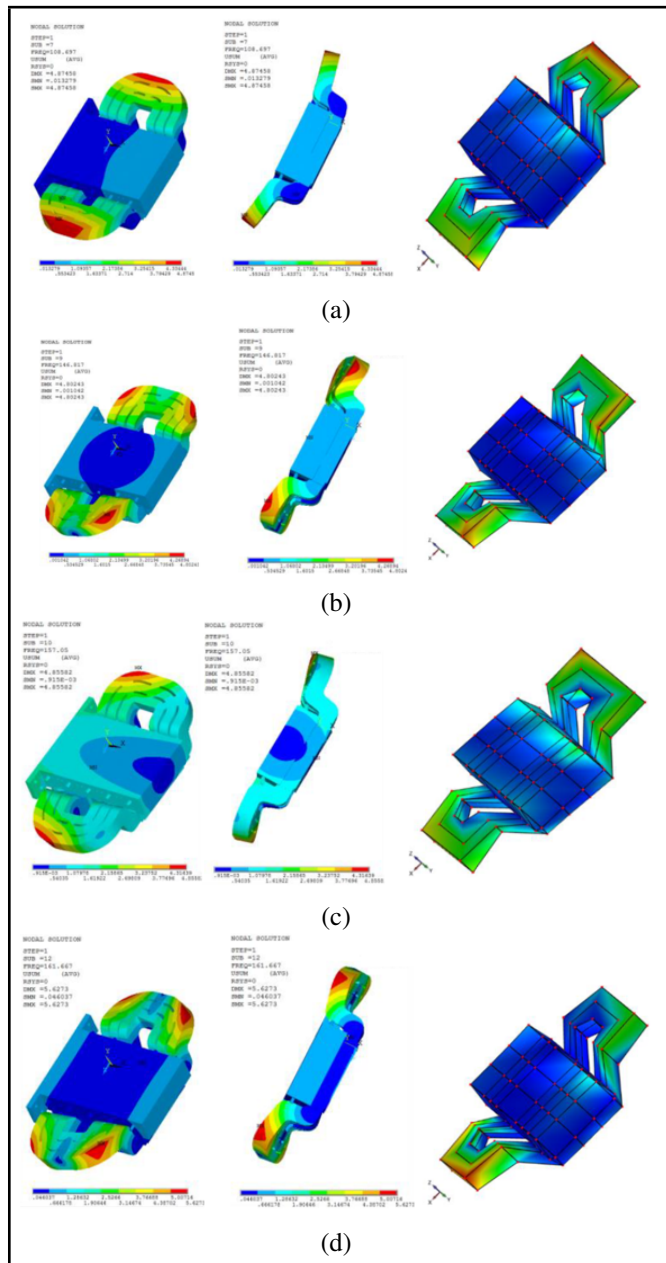


Figure 4. Comparison between Experiment and Simulation.(a) The first mode. (b) The second mode. (c) The third mode. (d) The fourth mode.

Table 2. Natural frequency of scaled stator.

Order	Natural frequency /Hz		Error /%
	Experiment	Simulation	
1	119.66	108.70	9.16
2	139.03	146.82	5.60
3	159.02	157.05	1.24
4	176.18	161.67	8.24
5	297.31	318.16	7.01
6	394.77	434.96	10.18

the model and calculation method.

2.3. Modal Analysis of Full-Size Motor

The modal characteristics of the superconducting motor stator assembly are assessed utilizing the hammer impact testing method. Comparing the overall formation of the stator assembly and the corresponding modal frequencies, the comparative simulation and test results are shown in Fig. 5 Analysis of the vibration patterns and corresponding frequencies in the com-

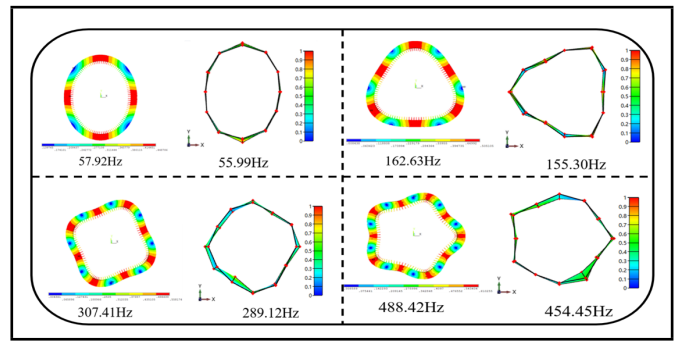


Figure 5. Comparison of simulation and test results.

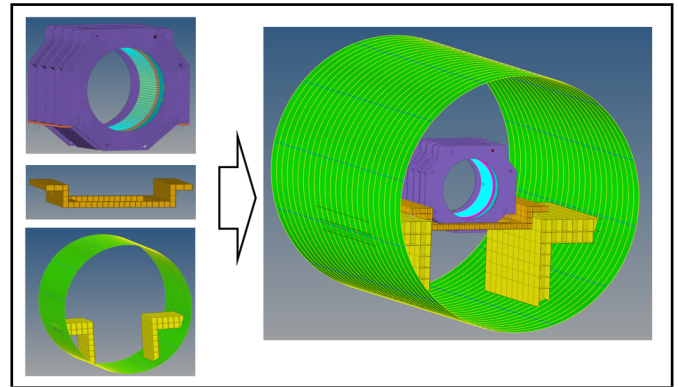


Figure 6. Finite element model of superconducting motor-raft-shell.

parative study between simulation and testing, as presented in Fig. 5, reveals a high degree of agreement between the results obtained from both methods.

3. VIBRATION CHARACTERISTICS ANALYSIS OF SUPERCONDUCTING MOTOR-RAFT-SHELL

The raft frame structure is devised as a lightweight plate frame structure, forming an integral part of the vibration isolation system along with the upper and lower vibration isolators, as depicted in Fig. 6. Setting the electromagnetic parameters in ANSYS Maxwell to obtain the electromagnetic force under the operating condition of the motor. The motor was set to rotate at a speed of 140 r/min in ANSYS Maxwell. After calculation, the magnetic field calculation results at a certain time, and the electromagnetic force curve under a certain cogging can be obtained. The basic process of obtaining electromagnetic force data is shown in Fig. 7. As shown in Fig. 7, under operating conditions of 140 rpm, the electromagnetic force in

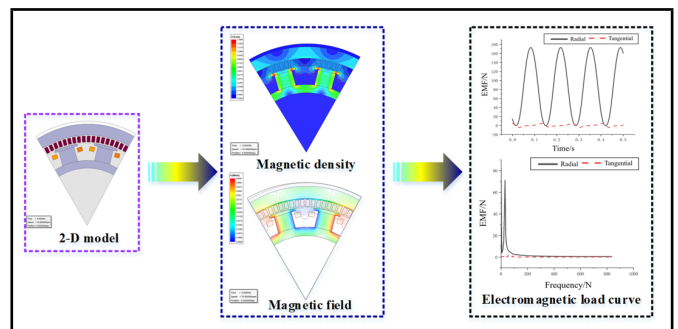


Figure 7. Flow chart of electromagnetic force calculation.

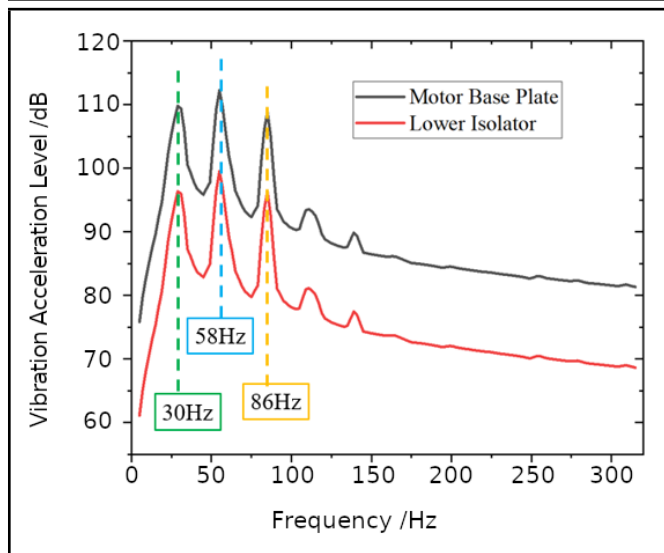


Figure 8. Vibration response curves at different positions of the motor.

the frequency domain exhibited its highest amplitude at 30 Hz. According to the relevant references, the structural damping of the superconducting motor-shell model was set to 0.001. The calculation frequency band was selected as 5 Hz - 315 Hz with a step size of 2 Hz. Calculating vibration response based on the full method. Two sets of measurement points were selected: motor base plate and lower isolator. Extract the vibration response of two sets of node groups and calculate the average value, and the curves are plotted as shown in Fig. 8. From Fig. 8, observed under the 140 rpm condition, the vibration response curves of the motor base plate and the lower vibration isolator exhibit a similar trend. The peak frequencies aligned closely with the excitation frequency of the motor's electromagnetic force (30 Hz) and the modal frequencies of the superconducting motor-shell system (58 Hz and 86 Hz). The resonance phenomenon was observed at 58 Hz due to its proximity to the second harmonic of the excitation force, resulting in a peak in the curve at that frequency. The synthesized vibration acceleration level at the motor base plate was 120.27 dB within the 5 Hz - 315 Hz frequency range, and at the lower isolator base, it is 106.64 dB. This double-layer vibration isolation configuration effectively reduces the transfer of vibration energy to the casing.

4. ANALYSIS OF VIBRATION TRANSMISSION PATH OF SUPERCONDUCTING MOTOR-RAFT-SHELL SYSTEM

To obtain the stiffness-matching design criterion of the vibration isolation system, it is also necessary to carry out the vibration transmission path analysis to clarify the vibration transmission law of the electromagnetic excitation on the motor itself and the raft frame. In this section, the vibration response of the motor-raft structure is calculated based on the finite element method, and the corresponding parameters can be extracted through post-processing, including the node stresses, node displacements, and node coordinates, then based on the extracted results, the power flow of a node on the shell can be calculated at a specific frequency,²¹ the calculation process is shown in Fig. 9. According to elasticity, the equations for the

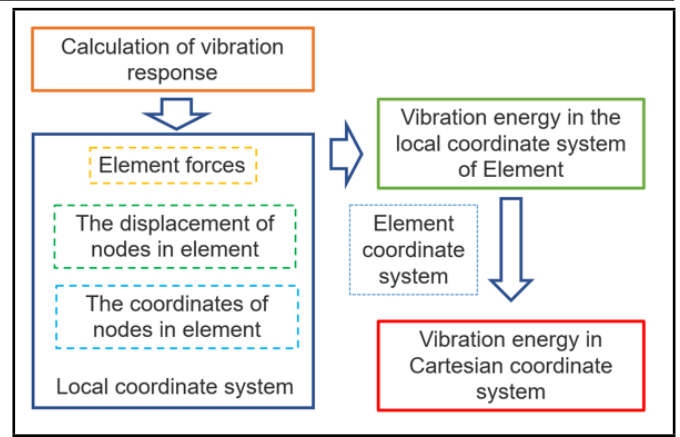


Figure 9. Structural sound intensity flow chart.

normal stress σ_x in the X direction, the normal stress σ_y in the Y direction, and the shear stress τ_{xy} in the plate shell structure can be expressed as deflection, which are:

$$\begin{cases} \sigma_x = \frac{E}{1-\mu^2} \left(\frac{\delta^2 w}{\delta x^2} + \mu \frac{\delta^2 w}{\delta y^2} \right) \\ \sigma_y = \frac{E}{1-\mu^2} \left(\frac{\delta^2 w}{\delta y^2} + \mu \frac{\delta^2 w}{\delta x^2} \right) \\ \tau_{xy} = \frac{E}{1+\mu} \frac{\delta^2 w}{\delta x \delta y} \end{cases} ; \quad (1)$$

In the formula, w represents the deformation of the shell element in the z-direction; μ Indicates Poisson's ratio; E represents the elastic modulus.

The calculation of the shell power flow also requires knowing the internal forces on the shell element, including the plane membrane force under longitudinal vibration and the bending moment, torque and shear force of the shell element under transverse vibration. Based on relevant theoretical derivation, expressions for membrane force, bending moment, torque, and shear force are obtained:

The formula for calculating the membrane force of shell elements is:

$$N_x = \int_{-t/2}^{t/2} \sigma_x dz = \frac{E}{1-\mu^2} \left(\frac{\delta u}{\delta x} + \mu \frac{\delta v}{\delta y} \right); \quad (2)$$

$$N_y = \int_{-t/2}^{t/2} \sigma_y dz = \frac{E}{1-\mu^2} \left(\frac{\delta v}{\delta y} + \mu \frac{\delta u}{\delta x} \right); \quad (3)$$

$$N_{xy} = N_{yx} = \int_{-t/2}^{t/2} \tau_{xy} dz = \frac{Et}{2(1+\mu)} \left(\frac{\delta u}{\delta y} + \mu \frac{\delta v}{\delta x} \right). \quad (4)$$

The formula for calculating the bending moment of the section is:

$$M_x = \int_{-t/2}^{t/2} \sigma_x z dz = -D \left(\frac{\delta^2 w}{\delta x^2} + \mu \frac{\delta^2 w}{\delta y^2} \right); \quad (5)$$

$$M_y = \int_{-t/2}^{t/2} \sigma_y z dz = -D \left(\mu \frac{\delta^2 w}{\delta x^2} + \frac{\delta^2 w}{\delta y^2} \right). \quad (6)$$

The formula for calculating cross-sectional torque is:

$$M_{xy} = M_{yx} = \int_{-t/2}^{t/2} \tau_{xy} z dz = -D(1-\mu) \frac{\delta^2 w}{\delta x \delta y}. \quad (7)$$

The formula for calculating cross-sectional shear force is:

$$Q_x = \int_{-t/2}^{t/2} \tau_{xy} dz = -D \left(\frac{\delta^3 w}{\delta x^3} + \frac{\delta^3 w}{\delta x \delta y^2} \right); \quad (8)$$

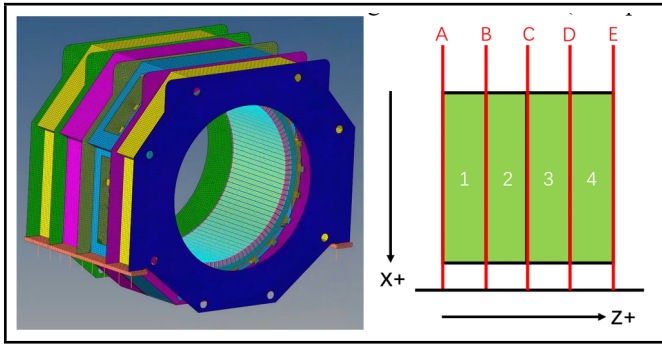


Figure 10. Simplified model of motor base.

$$Q_y = \int_{-t/2}^{t/2} \tau_{yz} dz = -D \left(\frac{\delta^3 w}{\delta x \delta y^2} + \frac{\delta^3 w}{\delta x^3} \right). \quad (9)$$

Based on the internal forces acting on the middle surface of the shell and the vibration response results obtained from finite element analysis, the structural intensity of the shell can be calculated. The calculation expression is:

$$I_x = \frac{-\omega}{2} \text{Im}(N_x u^* + N_{xy} v^* + Q_x w^* + M_x \theta_y^* - M_{xy} \theta_x^*); \quad (10)$$

$$I_y = \frac{-\omega}{2} \text{Im}(N_y v^* + N_{yx} u^* + Q_y w^* + M_y \theta_x^* - M_{yx} \theta_y^*); \quad (11)$$

In this formula: N_x and N_y are the axial forces in the X and Y directions; N_{xy} and N_{yx} are the shear forces of two-dimensional plates and shells; M_x and M_y are bending moments in the X and Y directions; M_{xy} and M_{yx} are the torques of two-dimensional plates and shells; Q_x and Q_y are the shear forces perpendicular to the plate and shell; u , v and w are displacements in the X, Y and Z directions; θ_x and θ_y are the angles of rotation in the X and Y directions; * represents complex conjugate; Im represents taking the imaginary part of the complex; ω represents circular frequency. The model structure of the superconducting motor-raft-shell system is complex, and the transfer path can be divided into two parts: the transmission path analysis at the motor base and the transmission path analysis at the middle raft.

4.1. Analysis of Transmission Path at the Motor Base

The motor base was simplified, and the motor base body unit was simplified into a shell unit, setting the same thickness and keeping the same mass. To clearly calibrate the transfer path, the simplified motor base was grouped and labeled, the vertical 5 panels were divided into A-E groups, and the vertical was divided into 1-4 groups, The model and schematic before and after simplification are shown in Fig. 10.

Based on the vibration response calculation results of the motor-raft-shell system model, the nodal internal forces and displacements of the motor seat shell unit group at a peak frequency of 58 Hz were extracted, and the structural acoustic intensity vector diagrams of each group are calculated through MATLAB programming, and the structural acoustic intensity contributions in the vertical direction (Groups A-E) and the longitudinal direction (Groups 1-4) are derived. From the structural sound intensity vector plot in Fig. 11, it can be seen that the structural sound intensity vector is more intensive in

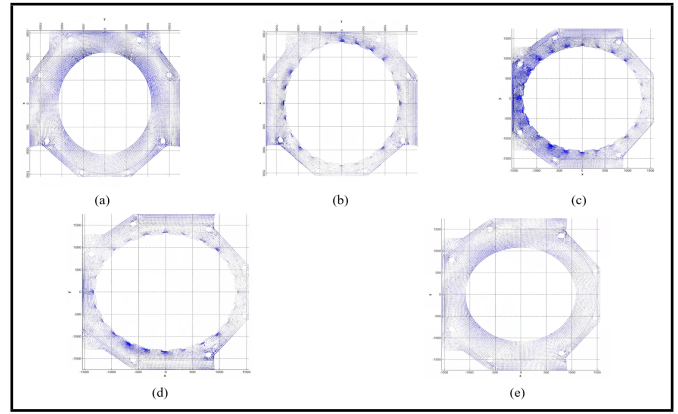


Figure 11. Vertical sound intensity vector diagram of each panel structure. (a)A Face. (b)B Face. (c)C Face. (d)D Face. (e)E Face.

Table 3. A-E plate structure sound intensity and contribution (X-direction).

Face	A	B	C	D	E
Structural intensity /W	0.1546	3.9023	74.7948	3.7342	0.2306
Contribution	0.001867	0.04712	0.903139	0.04509	0.002784

the C-surface, which proves that the vibration energy is transmitted in the C-surface, and the C-surface has the highest percentage of structural sound intensity contribution from the data in Table 3. Therefore, the electromagnetic force at the main peak frequency of 55 Hz is transmitted to the armature frame via the stator core, and then it is transmitted in the pendant panels mainly through the C-surface of the center to the base.

Observing the structural sound intensity vector diagram depicted in Fig. 12. It is evident that the structural sound intensity vectors are most pronounced on the 2 and 3 sides. This observation substantiates that vibration energy is predominantly transmitted in the longitudinal direction within these regions. Analysis of the data presented in Table 4 reveals that the structural sound intensity contributions from the 2 and 3 sides are comparable. Consequently, following the transmission of the electromagnetic force at the primary peak frequency of 55 Hz to the armature frame via the stator core, longitudinal propagation prevails primarily through the central 2 and 3 panels facing the base. In the motor chassis, the major pathway for vibration energy transmission is through the middle panel comprising the vertical C panel and longitudinal 2 and 3 panels down to the base.

4.2. Analysis of Transmission Path at the Raft Frame

In accordance with the structural sound intensity calculation process for the raft structure vibration transmission path analysis, to clearly analyze the transmission path, it was necessary to carry out a reasonable regional plate division, first of all, based on the composition of the raft structure was divided into the upper panel, the lower panel and the middle panel group, as shown in Fig. 13. The internal force, displacement, and coordinates of the nodes within each group of the raft frame were extracted at the peak frequency of 58 Hz, and the structural sound intensity vector diagrams of the upper, middle, and

Table 4. 1-4 Sound intensity and contribution of plate structure.

Face	1	2	3	4
Structural intensity /W	0.1826	5.5191	5.4377	0.2403
Contribution	0.01603	0.48502	0.47784	0.02111

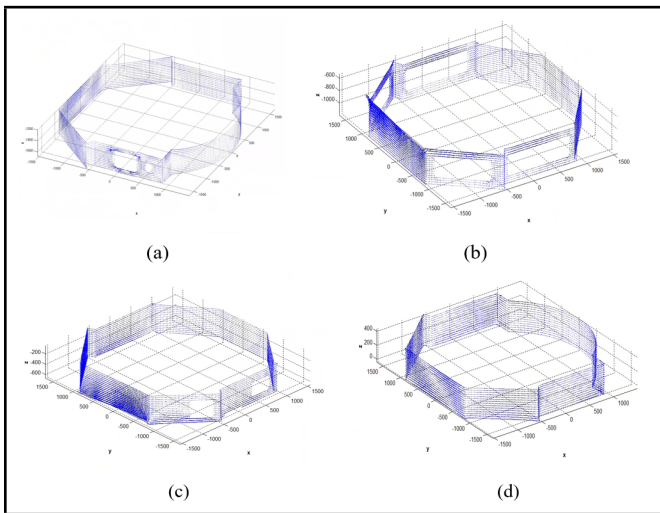


Figure 12. Vertical sound intensity vector diagram of each panel structure. (a)1 Face. (b)2 Face. (c)3 Face. (d)4 Face.

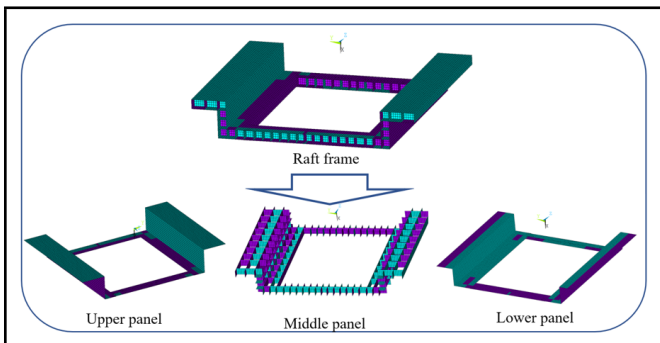


Figure 13. Schematic diagram of panel division of raft structure.

lower panels were plotted respectively, as shown in Fig. 14.

The excitation force from the motor propagates through the upper vibration isolator to the upper panel of the raft frame, subsequently transferring to the lower panel through the middle panel, and finally reaching the shell. Analysis of the sound intensity vector diagrams of each panel structure presented in Fig. 14 reveals that the energy distribution is symmetric due to the model’s symmetry. Notably, the diagonal energy is concentrated, while the middle energy is relatively sparse on the lower support plate, illustrating an uneven distribution of energy that elucidates the transfer of vibration energy from a structural perspective. This uneven distribution explains the transverse shaking state and larger deformations observed in the raft structure at peak frequencies.

5. DESIGN OF STIFFNESS MATCHING SCHEME FOR ISOLATOR

To address the problem of stiffness matching in the double-layer vibration isolator system of the motor-shell model, this section first clarifies the vibration energy transfer paths in the motor seat and raft frame based on the transfer path analysis. Based on this, different stiffness groups are designed, and different stiffnesses are assigned according to the size of the transfer contribution, and the vibration response agent model of the motor-shell under multiple groups of stiffness is established based on the RBF neural network, and finally, the optimal matching stiffness is selected based on the particle swarm op-

Table 5. Stiffness range for each group of vibration isolators

Stiffness (N/m)	Group 1	Group 2	Group 3	Group 4	Group 5	Group 6	
Y	Max	18800	37600	75200	18800	37600	75200
	Min	4700	9400	18800	4700	9400	18800
X	Max	102200	204400	408800	102200	204400	408800
	Min	25550	51100	102200	25550	51100	102200
Z	Max	8310	16260	32520	8310	16260	32520
	Min	2077.5	4155	8310	2077.5	4155	8310

timization algorithm. The technical route is shown in Fig. 15:

5.1. Division of Isolator Groups

The vibration isolator was simulated by a three-way spring, there are 9 pairs of upper- and lower-layer vibration isolators, and the middle pair was a separate group. according to this, the vibration isolators were divided into 3 groups from middle to both sides, and the upper and lower layers were divided into 6 groups. The specific grouping is shown in Fig. 16:

From the transmission path analysis, it can be seen that the vibration energy was mainly transmitted through the intermediate structure of the motor, relatively small stiffness can improve the vibration isolation efficiency²² and thus the intermediate group 1 and group 4 were given a lower stiffness, and the two sides of the stiffness is increased in turn, and each group was given a different stiffness is given a stiffness, the range is shown in Table 5. The vibration isolator was simulated by three-way spring, there were 9 pairs of upper- and lower-layer vibration isolators, and the middle pair was a separate group. according to this, the vibration isolators were divided into 3 groups from middle to both sides, and the upper and lower layers were divided into 6 groups. The specific grouping is shown in Fig. 16. From the transmission path analysis, it can be seen that the vibration energy is mainly transmitted through the intermediate structure of the motor, relatively small stiffness can improve the vibration isolation efficiency²² and thus the intermediate group 1 and group 4 were given a lower stiffness, and the two sides of the stiffness was increased in turn, and each group was given a different stiffness is given a stiffness, the range is shown in Table 5.

5.2. Establishment of an Electric Motor-Shell Agent Model

Taking the vertical, longitudinal, and lateral stiffness of the isolator as parameter inputs, the motor base plate vibration acceleration level and the lower end of the lower isolator vibration acceleration level as parameter output. A surrogate model for the superconducting motor raft shell system based on RBF neural network^{23,24} was established.

The establishment of the agent model needs to calculate the input and output of the model, and the selection of input parameters relies on the appropriate experimental design method, the experimental design method to set the parameters, the inputs, and to calculate the results, the outputs. Appropriate experimental design can save a lot of time. Frequently used experimental design methods include uniform experimental design method, central composite design, orthogonal design test, and so on. The uniform design test can be used without considering the neat comparability of the data without considering

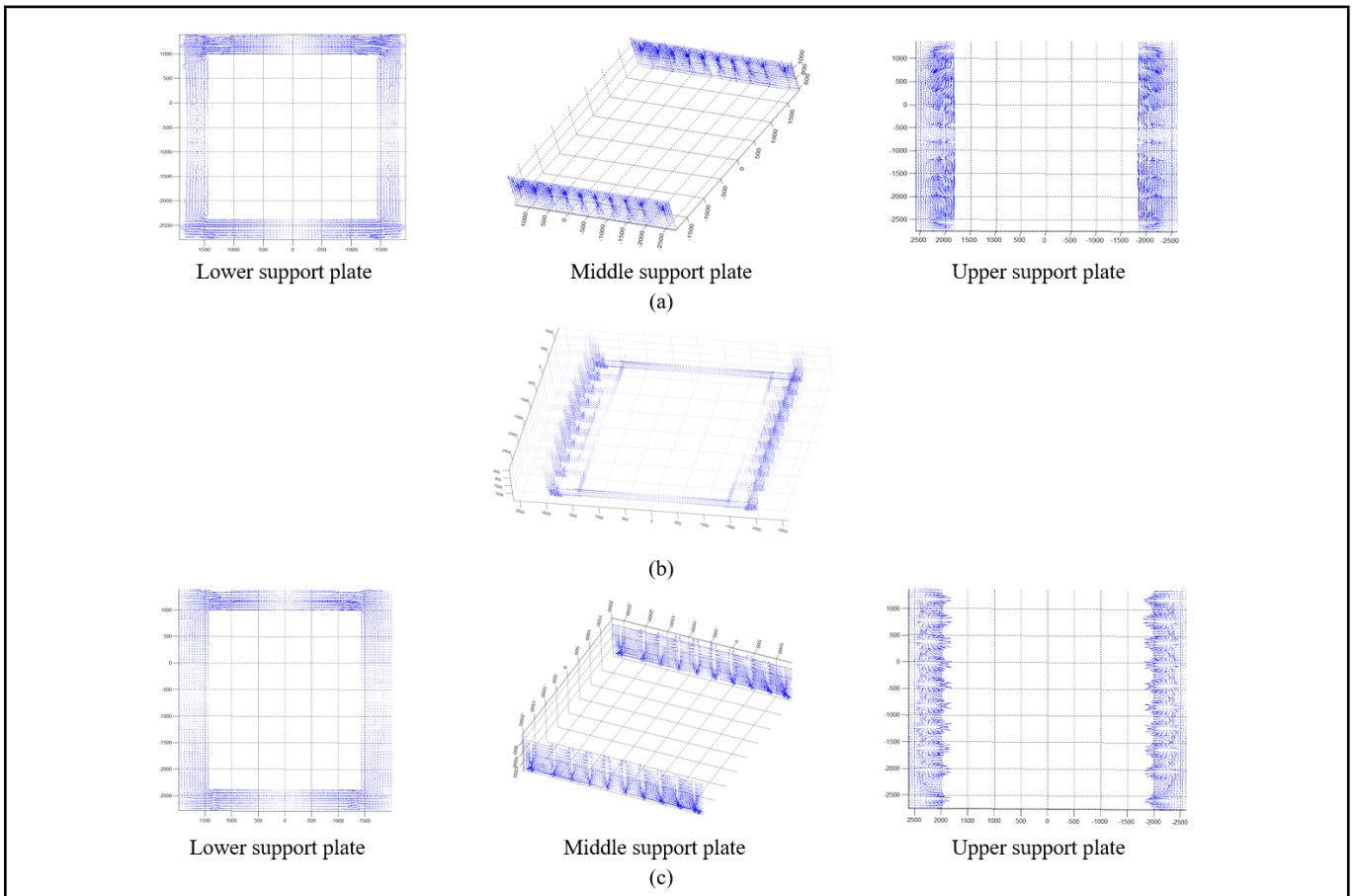


Figure 14. Sound intensity vector diagram of raft structure.(a)Upper Panel. (b)Middle Panel. (c)Lower Panel.

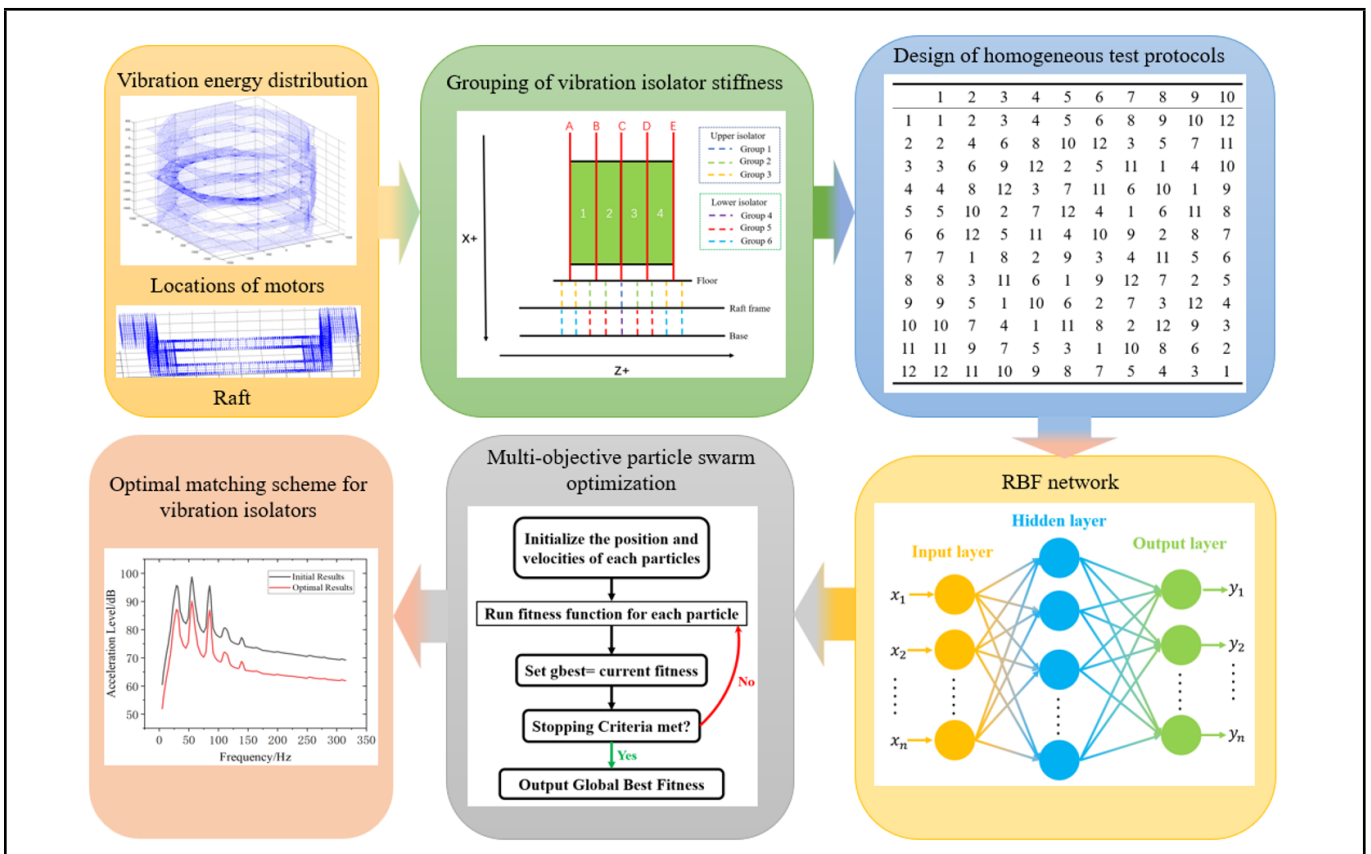


Figure 15. Flowchart for the design of the vibration isolator stiffness matching scheme.

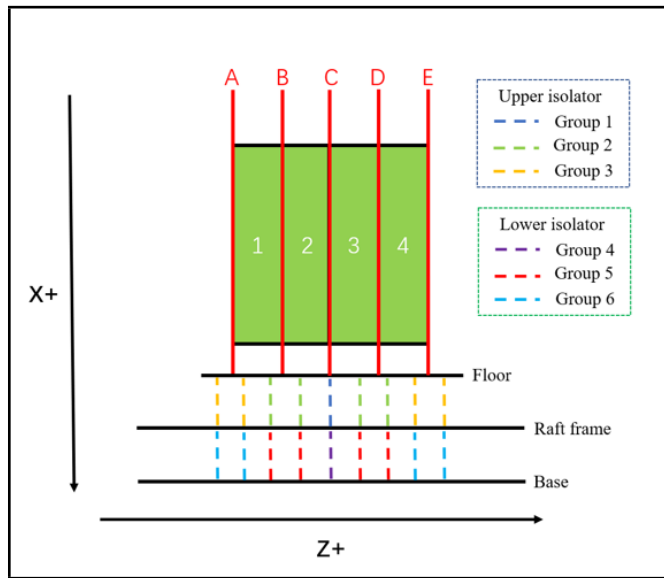


Figure 16. Schematic diagram of isolator grouping.

Table 6. $U_{12}(12^{10})$ Uniform Design Table.

	1	2	3	4	5	6	7	8	9	10
1	1	2	3	4	5	6	8	9	10	12
2	2	4	6	8	10	12	3	5	7	11
3	3	6	9	12	2	5	11	1	4	10
4	4	8	12	3	7	11	6	10	1	9
5	5	10	2	7	12	4	1	6	11	8
6	6	12	5	11	4	10	9	2	8	7
7	7	1	8	2	9	3	4	11	5	6
8	8	3	11	6	1	9	12	7	2	5
9	9	5	1	10	6	2	7	3	12	4
10	10	7	4	1	11	8	2	12	9	3
11	11	9	7	5	3	1	10	8	6	2
12	12	11	10	9	8	7	5	4	3	1

the order of magnitude of the parameters, so it has a wide range of applicability.

Based on the range of design variables to select the sample points, and the uniform experimental design method to design the experiment, based on the number of design variables, and the range of values, the experimental design was carried out by using the $U_{12}(12^{10})$ uniform design table, which is shown in Table 6, and the table of the use of $U_{12}(12^{10})$ is shown in Table 7. From the use table of $U_{12}(12^{10})$, it can be seen that the deviation of uniformity of the sample points for conducting 6-factor test was 0.2236, and the sample distribution of columns 1, 2, 6, 7, 8, and 9 in the design table of $U_{12}(12^{10})$ were selected in the test, and all the factors were selected to be the number of 12 levels. Using the uniform test design method to select different parameters of the working conditions, select 6 groups of vibration isolators in the vertical, longitudinal and transverse stiffness as the design variables, of which W_1 is the vibration acceleration level of motor base plate, W_2 is the vibration acceleration level of lower isolator. Setting the optimization of the design variables as shown in Table 8 – Table 10: Based on the MATLAB used to establish the superconducting motor-raft-shell system vibration response agent model, comparing the total level of vibration acceleration of the motor bottom plate and the lower vibration isolator end of the RBF neural network training iteration of the minimum error of 4.16×10^{-28} and 8.08×10^{-27} prediction curves are shown in Fig. 17:

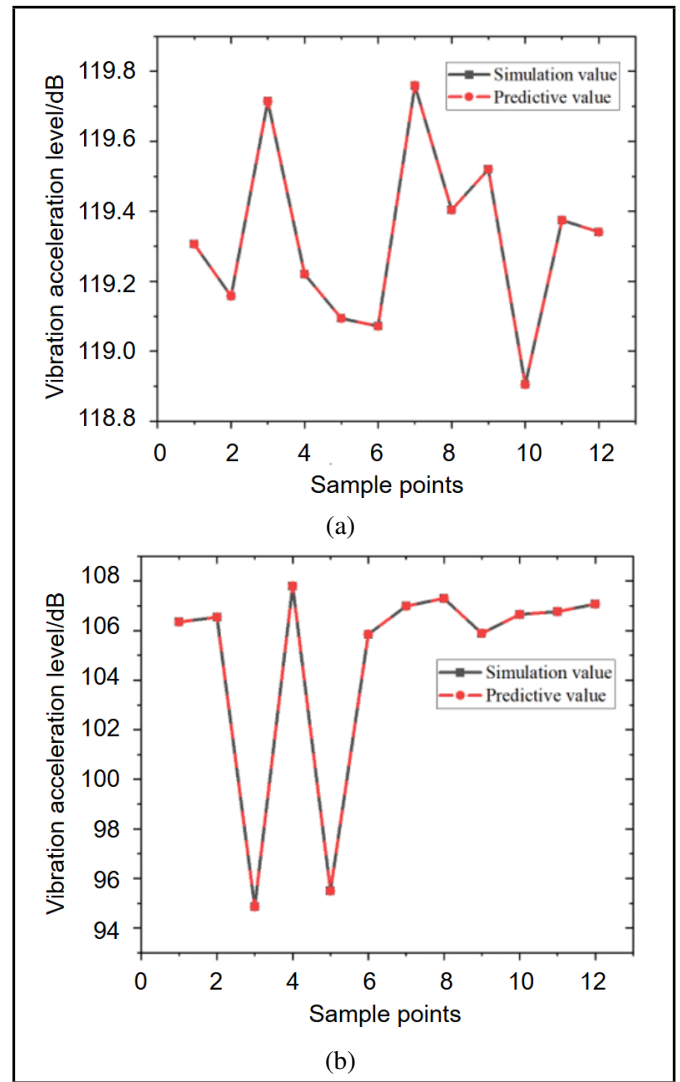


Figure 17. Prediction curve of RBF neural network. (a) Motor bottom plate. (b) The lower isolator.

5.3. Design of Stiffness Matching Scheme of Vibration Isolator Based on Multi-Objective Particle Swarm Optimization Algorithm

Multi-objective particle swarm algorithm (MOPSO) is an evolutionary computational algorithm for solving multi-objective optimization problems,²⁵ the basic idea of which is to transform multiple objective functions into a single comprehensive objective function and solve it using a particle swarm algorithm^{26,27} and is mostly used as an effective method to reduce the vibration amplitude of the objective.²⁸ To find an optimal solution, trade-offs and trade-offs between multiple objective functions are required, and Pareto fronts are an effective way to solve such problems. The Particle Swarm Optimization algorithm is a classical swarm intelligence optimization algorithm that achieves global optimization by updating the velocity and position of particles. In an M-dimensional search space, a group of N particles are initialized with random movements. After $k + 1$ iterations, the velocity and position update

Table 7. $U_{12}(12^{10})$ Use Table.

Number of factors	Column number	Uniformity deviation
2	1 5	0.116
3	1 6 9	0.184
4	1 6 7 9	0.223
5	1 3 4 8 10	0.227
6	1 2 6 7 8 9	0.267
7	1 2 6 7 8 9 10	0.277

Table 8. Experimental design scheme for training samples of vertical stiffness of isolators.

Operating conditions	Group 1	Group 2	Group 3	Group 4	Group 5	Group 6	W_1 / dB	W_2 / dB
1	25550	65036	241563	74327	162591	353054	119.31	106.35
2	32518	92909	408800	39486	106845	269436	119.16	106.54
3	39486	120782	213691	95232	51100	185818	119.71	99.86
4	46455	148655	380927	60391	176527	102200	119.22	107.80
5	53423	176527	185818	25550	120782	380927	119.09	100.50
6	60391	204400	353054	81295	65036	297309	119.07	105.85
7	67359	51100	157945	46455	190464	213691	119.76	106.99
8	74327	78973	325182	102200	134718	130073	119.40	107.29
9	81295	106845	130073	67359	78973	408800	119.52	105.89
10	88264	134718	297309	32518	204400	325182	118.90	106.65
11	95232	162591	102200	88264	148654	241564	119.37	106.76
12	102200	190464	269436	53423	92909	157945	119.34	107.07

Table 9. Experimental design scheme for lateral stiffness training samples of isolators.

Operating conditions	Group 1	Group 2	Group 3	Group 4	Group 5	Group 6	W_1 / dB	W_2 / dB
1	4700	11964	44436	13673	29909	64945	119.31	106.35
2	5982	17091	75200	7264	19654	49564	119.16	106.54
3	7264	22218	39309	17518	9400	34182	119.71	99.86
4	8545	27345	70073	11109	32473	18800	119.22	107.80
5	9827	32473	34182	4700	22218	70073	119.09	100.50
6	11109	37600	64945	14954	11964	54691	119.07	105.85
7	12391	9400	29055	8545	35036	39309	119.76	106.99
8	13673	14527	59818	18800	24782	23927	119.40	107.29
9	14955	19654	23927	12391	14527	75200	119.52	105.89
10	16236	24782	54691	5982	37600	59818	118.90	106.65
11	17518	29909	18800	16236	27345	44436	119.37	106.76
12	18800	35036	49564	9827	17091	29054	119.34	107.07

Table 10. Experimental design scheme for training samples of longitudinal stiffness of isolators.

Operating conditions	Group 1	Group 2	Group 3	Group 4	Group 5	Group 6	W_1 / dB	W_2 / dB
1	2077	5255	19314	6044	12959	28118	119.31	106.35
2	2644	7456	32520	3211	8557	21515	119.16	106.54
3	3211	9657	17114	7743	4155	14913	119.71	99.86
4	3777	11858	30319	4910	14059	8310	119.22	107.80
5	4344	14059	14913	2077	9657	30319	119.09	100.50
6	4910	16260	28118	6610	5255	23716	119.07	105.85
7	5477	4155	12712	3777	15159	17114	119.76	106.99
8	6044	6356	25917	8310	10758	10511	119.40	107.29
9	6610	8557	10511	5477	6355	32520	119.52	105.89
10	7177	10758	23716	2644	16260	25917	118.90	106.65
11	7743	12959	8310	7177	11858	19314	119.37	106.76
12	8310	15159	21515	4344	7456	12712	119.34	107.07

formulas for particle $i = 1, 2, \dots, N$ are as follows:

$$v_i^{k+1} = \omega v_i^k + c_1 rand_1(P_{best_i}^k - x_i^k) + c_2 rand_2(g_{best}^k - x_i^k); \quad (12)$$

$$x_i^{k+1} = x_i^k + v_i^k; \quad (13)$$

In the formulas, v_i^{k+1} represents the velocity of particle i at the $k + 1$ -th iteration; x_i^{k+1} represents the position of particle i at the $k + 1$ -th iteration; $P_{best_i}^k$ represents the historical best position of particle i up to the k -th iteration; g_{best}^k represents the historical best position of all particles up to the k -th iteration; ω is the inertia weight, which adjusts the global optimization and local optimization abilities of the particles; c_1 and c_2 are the learning factors that control the optimization speed of the particles; $rand_1$ and $rand_2$ are uniformly distributed random numbers within a certain interval, which prevent particles from getting trapped in local optima.

The particles in the MOPSO algorithm represent the candidate solutions, and each particle contains a position vector and a velocity vector, and the position and velocity of each particle are updated through continuous iterations, and in each iteration, the optimal candidate solution is selected by comparing the position vector and velocity vector of each particle. To find an optimal solution, trade-offs and trade-offs between multiple objective functions are required, and Pareto fronts are an effective way to solve such problems. Therefore, in this section, the MOPSO algorithm is invoked based on the MATLAB programming, and the artificial neural network module is used to complete the data fitting and update the Pareto frontiers, and finally the global pareto frontiers of the two objective functions are obtained. The optimization objective function is as follows:

$$find \begin{cases} \min W_1 \\ \min W_2 \end{cases}; \quad (14)$$

In this formula: W_1 is the vibration acceleration level of motor base plate, W_2 is the vibration acceleration level of lower isolator. The needle will be trained RBF neural network prediction model as the fitness function, using a multi-objective particle swarm algorithm to solve the multi-objective optimization mathematical model. The parameters of the multi-objective particle swarm algorithm are set as follows: the population size is 200, the maximum number of iterations of the algorithm is 500, the values of the learning factors and are 2, and the inertia weight ω is 0.9. The pareto front obtained by the algorithm solution is shown in Fig. 18. Based on the design criterion of minimizing the vibration transmitted to the shell, the optimal stiffness matching scheme is selected as shown in Tab. 11, and the layout of the vibration isolator stiffness presents the characteristics of low stiffness in the middle and high stiffness on both sides, and the stiffness of the lower vibration isolator is higher than that of the upper vibration isolator. According to the six optimal stiffness matching schemes selected, the stiffness of the vibration isolation system is designed, and the vibration response of the superconducting motor-raft-shell system model is calculated under the optimal stiffness, and the synthetic curves of vibration acceleration levels of the motor bottom plate and the lower end of the lower vibration isolator are extracted and compared with the initial results as shown in Fig. 19. Synthesize the vibration acceleration levels within

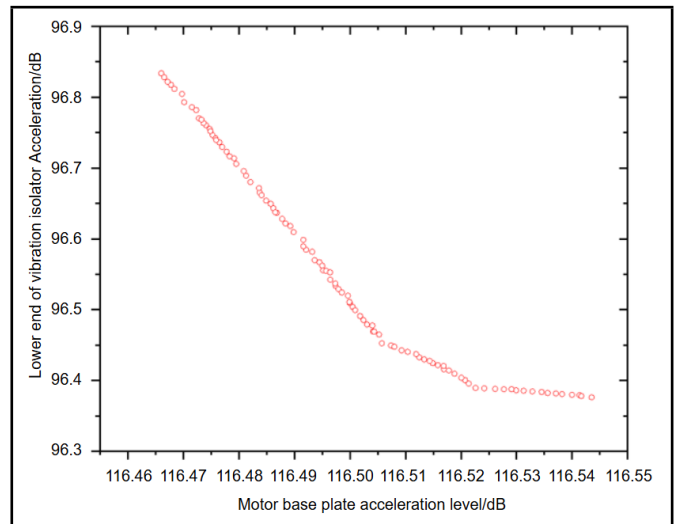


Figure 18. Multi-objective particle swarm algorithm - Pareto frontiers.

Table 11. Selection of optimal stiffness matching scheme.

Group	Group 1			Group 2			Group 3		
Direction	X	Y	Z	X	Y	Z	X	Y	Z
Stiffness (N/mm)	25550	4700	2078	204400	37600	16260	408800	75200	32520
Group	Group 4			Group 5			Group 6		
Direction	X	Y	Z	X	Y	Z	X	Y	Z
Stiffness (N/mm)	102200	18800	8310	162591	29909	12959	408800	162591	32520

the 5 Hz - 315 Hz frequency range, and organize the table as shown in Table 12: As depicted in Table 12, the optimization process results in a reduction of 8.6 dB in the vibration levels at the lower end of the vibration isolator, while the vibration levels of the motor base plate remain unchanged. The relative errors between the algorithm's optimized values and the simulation-based optimized values are found to be 1.42 % and 1.19 % respectively, falling within the acceptable range in engineering. This optimization scheme effectively diminishes the vibration propagated to the motor shell from the motor excitation force by adopting a rational matching strategy for the vibration isolator, with the vibration levels at the motor bottom plate remaining essentially unaffected. By implementing an appropriate vibration isolator stiffness matching scheme while ensuring the stability of the motor base plate vibration levels, the transmission of vibration to the motor shell from the motor excitation is significantly reduced

6. CONCLUSIONS

In this study, a matching scheme for multi-stiffness isolators of the superconducting motor isolation vibration system is established based on the RBF neural network surrogate model and multi-objective particle swarm optimization algorithm to address the issue of increased shell vibration due to resonance. Additionally, a numerical simulation model of the supercon-

Table 12. Comparison of optimization results.

	Composition acceleration value of motor base plate /dB	Acceleration synthesis at the lower end of the isolator /dB
Initial value	120.27	106.64
Optimal value	116.95	96.87
Simulation value	118.63	98.04

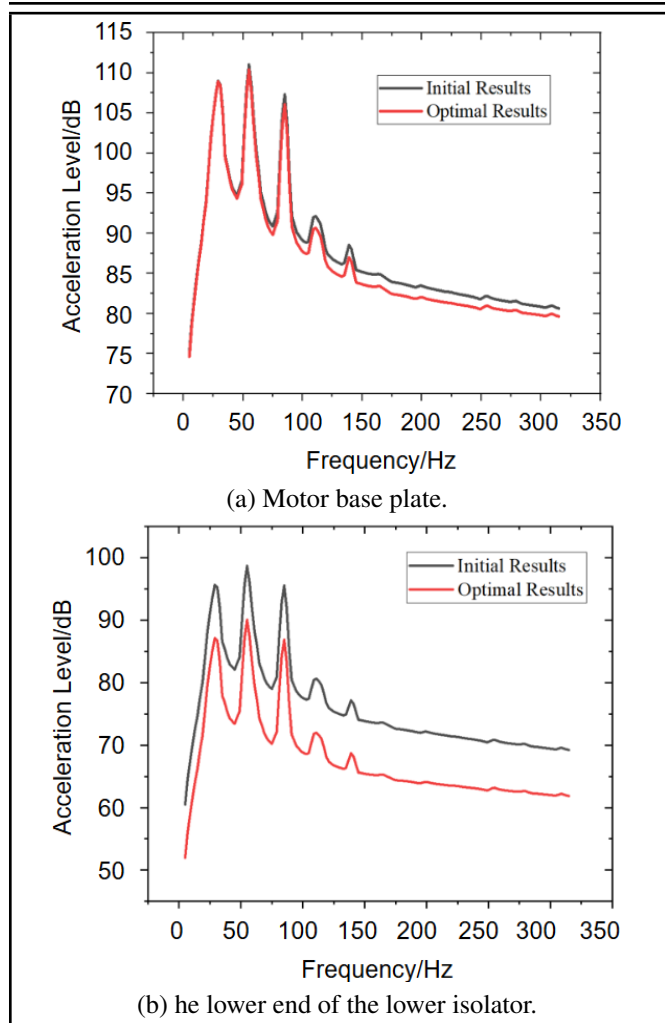


Figure 19. Comparison of vibration acceleration level curves of different positions before and after optimization.

ducting motor-raft-shell system is developed using the finite element method. The accuracy of the simulation model is validated through stator experiments, and the propagation pathways and energy distribution density of electromagnetic forces on the superconducting motor structure and raft are analyzed using the structural intensity analysis. The key findings of this investigation are summarized as follows:

1. A modeling approach for simplifying the stator assembly of superconducting motors was proposed, and its validation is conducted through modal testing. The error between simulation and experimental results did not exceed 8 %, meeting the requirements for simulation calculations.
2. The vibration peaks of the superconducting motor-raft-shell system model under the 140 rpm operating condition are mainly distributed at the excitation frequency of electromagnetic forces, their harmonics, and the motor modal frequencies. The highest amplitude occurs at 58 Hz due to system resonance. Therefore, when designing the stiffness of motor support isolation vibration, it is necessary to avoid the coincidence of motor installation frequency with the excitation frequency and its harmonics.
3. The analysis of the transmission path reveals that the electromagnetic excitation force propagates from the sta-

tor system to the intermediate chassis and subsequently to the motor base plate. Within the raft structure, the non-uniform distribution of vibration energy on the upper panel due to its middle hollowing design leads to increased raft vibration displacement. Vibration energy is predominantly transmitted through the central transverse and longitudinal panels, with a more uniform energy distribution observed at the lower panel support .

4. The optimal stiffness matching scheme for the vibration isolation system is developed based on the RBF neural network and the multi-objective particle swarm optimization algorithm. The stiffness distribution pattern of the isolators in the isolation vibration system exhibits a characteristic of "soft in the middle, hard on both sides," with the stiffness of the lower isolator greater than that of the upper isolator. The design scheme is validated through numerical simulations, with a vibration error of less than 2 % achieved. Under the optimal stiffness matching scheme, the vibration transmitted from the motor to the shell is reduced by 8.6 dB. This effectively mitigated the vibration transmitted from the electromagnetic force to the hull while maintaining the motor's vibration unchanged.

ACKNOWLEDGEMENTS

This work was supported by the National Natural Science Foundation of China ('Research on complex composite shell fluid-solid coupling low frequency vibration and acoustic radiation combined with seaward fluid disturbing mechanism', Grant No.52241102).

REFERENCES

- ¹ Fernando, J., Monteiro, D., et al., Performance Comparison of Superconducting Machines With Induction Motors, *IEEE Transactions on Applied Superconductivity*, **32**(7), 1-5,(2022). <https://doi.org/10.1109/TASC.2022.3188461>
- ² Liu, Z., Xiang, Y., Zhou, Y., Research on the Influence of Silicon Steel Sheet Stacking on HTS Motor Stator Core Modal, *IEEE International Conference on Applied Superconductivity and Electromagnetic Devices*, 16-18, (2020). <https://doi.org/10.1109/ASEMD49065.2020.9276189>
- ³ Wang, Y.B., Zhao, C.C., et al., Vibroacoustic Prediction of a High-Temperature Superconducting Field-Modulation Double-Stator Machine with Stationary Seal, *Energies*, **11**(10), 2563, (2018). <https://doi.org/10.3390/en11102563>
- ⁴ Chai, F., Li, Y., et al., Accurate modelling and modal analysis of stator system in permanent magnet synchronous motor with concentrated winding for vibration prediction, *IET Electric Power Applications*, **12**(8), 1225-1232, (2018). <https://doi.org/10.1049/iet-epa.2017.0813>
- ⁵ Yin, H.B., Ma, F.W., Zhang, X.Y., et al., Research on equivalent material properties and modal analysis method of stator system of permanent magnet motor with concentrated winding, *IEEE Access*, **7**, 64592-64602, (2019). <https://doi.org/10.1109/ACCESS.2019.2916428>

- ⁶ Yu, H., Tian, L., Zhang, G., Transfer Path Analysis of Structural Vibration on Propulsion Motor, *IEEE International Magnetics Conference*, **51**(11), 1-3, (2015). <https://doi.org/10.1109/TMAG.2015.2453212>
- ⁷ Li, M., Liu, Q., Dai, G., Chen, W., Zhu, R., Vibration Transfer Path Analysis of Double-Layer Box for Marine Reducer, *Journal of Vibration Engineering & Technologies*, **9**(6), 1077-1089, (2021). <https://doi.org/10.1007/s42417-021-00283-0>
- ⁸ Yang, Y., Pan, G., Yin, S., Yuan, Y., Vibration transmission path analysis of underwater vehicle power plant based on TPA power flow, *Proceedings of the Institution of Mechanical Engineers, Part M: Journal of Engineering for the Maritime Environment*, **236**(1), 150-159, (2022). <https://doi.org/10.1177/14750902211024068>
- ⁹ Wang, L., Chen, T., Structural intensity analysis of the cantilevered plate under thermal load, *THIN-WALLED STRUCTURES*, **139**, 209-218, (2019). <https://doi.org/10.1016/j.tws.2019.03.017>
- ¹⁰ Zhu, C., Li, G., Ruan, S., Yang, J., Structural Intensity of Laminated Composite Plates Subjected to Distributed Force Excitation, *Journal of Vibration Engineering and Technologies*, **11**(6), 2779-2791, (2023). <https://doi.org/10.1007/s42417-023-00909-5>
- ¹¹ Yasa, Y., Sozer, Y., et al., Acoustic Noise Mitigation of Switched Reluctance Machines With Leaf Springs, *IEEE Transactions on Industrial Electronics*, **70**(2), 1250-1260, (2023). <https://doi.org/10.1109/TIE.2022.3159969>
- ¹² Husaini, R., Riantoni, R., Nurdin, N., et al., Failure Analysis of the Leaf Spring of Truck Colt Diesel Using Finite Element Method, *IOP Conference Series: Materials Science and Engineering*, **547**(1), 012017, (2019). <https://doi.org/10.1088/1757-899X/547/1/012017>
- ¹³ Li, Y., Zhu, C., Multi-Objective Optimal Design of μ -Controller for Active Magnetic Bearing in High-Speed Motor, *Actuators*, **12**(206), 206, (2023). <https://doi.org/10.3390/act12060206>
- ¹⁴ Zhao, H., Li, D., et al., Research on vibration suppression method of alternating current motor based on fractional order control strategy, *PROCEEDINGS OF THE INSTITUTION OF MECHANICAL ENGINEERS PART E-JOURNAL OF PROCESS MECHANICAL ENGINEERING*, **231**(4), 786-799, (2017). <https://doi.org/10.1177/0954408916637380>
- ¹⁵ Li, Q., Liu, S., et al., Sideband Vibration Suppression of Interior Permanent Magnet Synchronous Motors for Electric Vehicles Under Multiple Operating Conditions, *IEEE Transactions on Transportation Electrification*, **9**(1), 322-335, (2023). <https://doi.org/10.1109/TTE.2022.3160347>
- ¹⁶ Wang, M., Chai, K., et al., Shi. Dynamic characteristics and experimental study of double layer vibration isolation system, *Journal of Mechanical Science and Technology*, **37**(4), 1-11, (2022). <https://doi.org/10.1007/s12206-023-0311-2>
- ¹⁷ Wen, X., Li, W., et al., Design and Vibration Isolation Performance of Truss-Type CFRP Raft Frame, *Shock & Vibration*, **2019**(1), 1-10, (2019). <https://doi.org/10.1155/2019/4281958>
- ¹⁸ He, D., Wang, Q., et al., Vibration analysis of functionally graded material (FGM) double layered floating raft structure by the spectro-geometric method, *Structures*, **48**, 533-550, (2023). <https://doi.org/10.1016/j.istruc.2022.11.111>
- ¹⁹ Li, Y., Xu, D., Vibration attenuation of high dimensional quasi-zero stiffness floating raft system, *International Journal of Mechanical Sciences*, **126**, 186-195, (2017). <https://doi.org/10.1016/j.ijmecsci.2017.03.029>
- ²⁰ Wang, Z., Mak, C., Optimization of geometrical parameters for periodical structures applied to floating raft systems by genetic algorithms, *Applied Acoustics*, **129**, 108-115, (2018). <https://doi.org/10.1016/j.apacoust.2017.07.018>
- ²¹ Tian, X., Liu, G., et al., Crack detection in offshore platform structure based on structural intensity approach, *Journal of Sound and Vibration*, **389**, 236-249, (2017). <https://doi.org/10.1016/j.jsv.2016.11.020>
- ²² Vo, N., Nguyen, M., Le, T., Analytical study of a pneumatic vibration isolation platform featuring adjustable stiffness, *Communications in Nonlinear Science & Numerical Simulation*, **98**, 105775, (2021). <https://doi.org/10.1016/j.cnsns.2021.105775>
- ²³ Syed, M., Khan, S., et al., Multi-Kernel Fusion for RBF Neural Networks, *Neural Processing Letters*, **55**(2), 1045-1069, (2023). <https://doi.org/10.1007/s11063-022-10925-3>
- ²⁴ Guo, J., Wang, M., et al., Prediction of Ship Cabin Noise Based on RBF Neural Network, *Mathematical Problems in Engineering*, **2019**(1), 1-21, (2019). <https://doi.org/10.1155/2019/2781437>
- ²⁵ Zheng, L., Yang, X., Chen, S., Optimization-based Improved Kernel Extreme Learning Machine for Rolling Bbearing Fault Ddiagnosis, *Brazilian Society of Mechanical Sciences and Engineering*, **2019**, 1-14, (2019). <https://doi.org/10.1007/s40430-019-2011-5>
- ²⁶ Li, L., Liang, C., Gu, T., Sheng, W., Wang, W., On the Norm of Dominant Difference for Many-Objective Particle Swarm Optimization, *IEEE Transactions On Cybernetics*, **51**(4), 2055-2067, (2021). <https://doi.org/10.1109/TCYB.2019.2922287>
- ²⁷ Trivedi, V., Varshney, P., Ramteke, M., A simplified multi-objective particle swarm optimization algorithm, *Swarm Intelligence*, **1**, 1-34, (2019). <https://doi.org/10.1007/s11721-019-00170-1>
- ²⁸ Sun, W., Ma, H., et al., Multi-objective optimization of cylindrical shell structure with local viscoelastic damping patch for minimum vibration response and lightest attachment mass, *Structural and Multidisciplinary Optimization*, **65**(11), 1-28, (2022). <https://doi.org/10.1007/s00158-022-03418-3>